Proceedings of the 11th ICPMG 2026
11th International Conference on Physical Modelling in Geotechnics
8-12 June 2026, Zurich, Switzerland

Centrifuge modelling of a high embankment under seismic motions: LEAP-ASIA 2025 tests at Kansai University

H.K. Hong
Kansai University, Suita, Japan, k561984@kansai-u.ac.jp

T. Tobita, M. Kunisawa, H.Tobe
Kansai University, Suita, Japan, tobita@kansai-u.ac.jp, k763211@kansai-u.ac.jp, k570174@kansai-u.ac.jp

ABSTRACT: As part of LEAP-ASIA-2025, centrifuge model experiments and finite element analyses were conducted at Kansai University to investigate the seismic response of a uniform embankment founded on ground with relative densities of 50% and 70%. In the centrifuge experiments, generalised scaling laws were applied in addition to standard centrifuge scaling, and prototype-scale numerical analyses were validated against the experiments. Supplementary investigations were also performed by applying an impermeable surface layer to examine partially drained conditions. Generalised scaling-law-based centrifuge experiments showed good agreement with prototype-scaled numerical analyses as relative density increased, and overburden stress decreased. The partially drained condition resulted in a pronounced delay in the dissipation of excess pore water pressure, suggesting that, in impermeable surface conditions representative of natural urban ground, the duration of liquefaction-induced strength reduction may differ from that predicted by idealised experimental and numerical models.

1 INTRODUCTION

Earthquake-induced ground liquefaction beneath embankments is a major geohazard. Post-earthquake investigations have shown that embankments and river dikes founded on loose, liquefiable sandy soils are particularly vulnerable during earthquakes (Sasaki et al., 2012; Chiaradonna et al., 2019; Tsai et al., 2018).

Despite advances in experimental and numerical modelling of embankment-foundation systems affected by liquefaction, reproducing liquefaction behaviour under seismic loading remains challenging, owing to the complex nature of liquefaction processes.

LEAP (Liquefaction Experiments and Analysis Project) is an international collaborative effort aimed at validating numerical predictions of soil liquefaction through centrifuge tests conducted using standardised protocols across multiple institutions, thereby providing a consistent framework for model validation (Kutter et al., 2019; Tobita et al., 2024).

Within this framework, LEAP-ASIA-2025 is conducted as a coordinated research phase focusing on embankment–foundation systems. In this phase, centrifuge experiments and numerical analyses are performed for a common embankment configuration, while foundation ground conditions vary across participating institutions. This study investigates liquefaction behaviour in foundation ground with relative densities of 50% and 70%. Supplementary experimental and numerical investigations were conducted to evaluate partially drained conditions by applying an impermeable layer at the ground surface.

2 METHODS

2.1 LEAP-ASIA-2025 Experiments

Geotechnical centrifuge experiments were conducted at Kansai University, Japan, using a 1.5 m radius centrifuge at 50 G. The experimental model was placed in a rigid box (45 cm × 20 cm × 40 cm).

Material properties and grain size distributions of the Ottawa sand used for the foundation and the Silica No. 3 sand used for the embankment are presented in Table 1 and Figure 1, respectively.

Figure 2 illustrates the schematic experimental model, with prototype-scale dimensions on the left and model-scale dimensions on the right (italicised). The relationship between the prototype and model scales is defined by the 50 G centrifuge scaling combined with a generalised scaling law applied to a model reduced by a factor of 1.6. To visually observe deformation behaviour, soba noodles were arranged in a grid pattern along the transparent window of the rigid box. A surface curve corresponding to the rotation radius was applied symmetrically to the model to impose a uniform centrifugal acceleration across the ground under the 50 G condition (Tobita et al., 2018); this curve is omitted on the prototype-scale side. To minimise the influence of saturation variability, a constant amount of surface water was applied using the same fluid as that used for foundation saturation.

Seven accelerometers and six pore pressure transducers were installed at depths corresponding to one-half and one-quarter of the foundation depth, distributed from beneath the embankment centre to the free-field region to capture embankment-induced loading conditions. Table 2 summarises the specifications and manufacturers of the sensors used in the experiments. Sensor selection was constrained by operational feasibility under the given experimental conditions. In the A5 region, where the largest foundation deformation was expected, small-sized accelerometers were employed to minimise disturbances caused by sensor volume. For the same reason, small pore pressure transducers were installed at locations near the ground surface (P1, P3, and P5). All sensors were installed with slight adjustments in sensor depth to account for variations in the rotation radius. Input acceleration (A0) was measured outside the rigid box.

Table 3 summarises the experimental cases of this study. Case 1 is the reference condition, with the foundation ground prepared at 50% relative density, while Case 2 employs a higher relative density of 70%. Case 3 uses the same foundation condition as Case 1 and introduces a partially drained condition by applying a 0.5 m-thick Ottawa sand layer saturated with a high-viscosity fluid (45,000 cSt). The foundation ground was prepared by air pluviation to achieve the target relative densities and saturated in a vacuum chamber using a methylcellulose solution (Shin-Etsu Chemical Co., Ltd., 2005) with a kinematic viscosity of 71.2 cSt. This viscosity of the fluid was selected to satisfy the generalised scaling law (Tobita et al., 2022). Table 4 shows the scaling factors applied in this study for 1 g scaling laws, centrifugal field, and combined generalised scaling.

The embankment model was constructed from Silica No. 3 sand at an initial relative density of 90% using a mould. After saturation with the same 71.2 cSt viscous fluid, the embankment was frozen to preserve its geometry; however, trimming of the embankment base was required due to volumetric expansion during freezing, resulting in a final relative density of 80%.

For Case 3, in which the surface water was a high-viscosity fluid, the embankment was constructed manually without freezing using Silica No. 3 sand, with mass corresponding to 80% relative density.

Figure 3 shows the applied input acceleration, provided from LEAP-ASIA-2025.

Table 1. Ottawa and Silica No. 3 sand material properties.

Properties	Ottawa	Silica No. 3
Specific gravity G_s	2.65	2.64
Min void ratio e_{min}	0.49	0.69
Max void ratio e_{max}	0.74	0.95
Max dry density ρ_{max} (Mg/m^3)	1.75	1.56
Min dry density ρ_{min} (Mg/m^3)	1.45	1.35

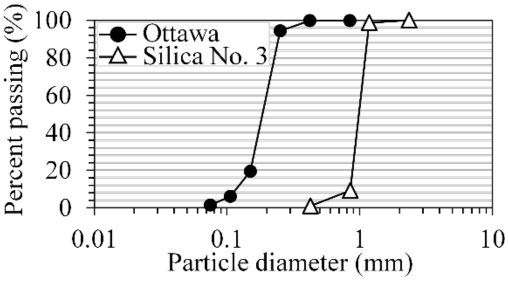

Figure 1. Grain size distribution curves of Ottawa sand (Kutter et al., 2019) and Silica No. 3 sand.

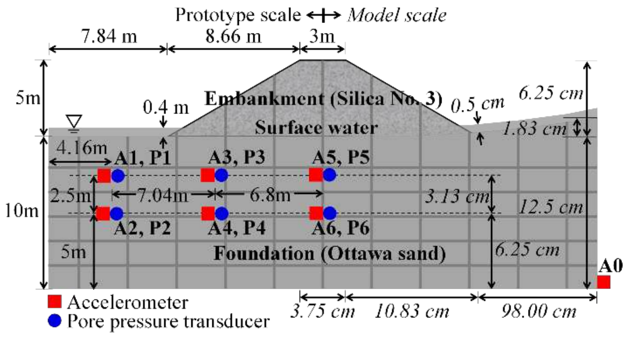

Figure 2. Schematic diagram of the experimental model.

Table 2. Utilised sensors in experiments.

Type	Specification (mm)	Manufacturer (model)
A0-A4, A6	16×16×28	TML (ARH-500A)
A5	6×6×6	SSK (A6H-50G)
P1, P3, P5	ϕ12×8	SSK (P310A-2)
P2, P4, P6	ϕ20×35	KYOWA (BPR-A-200KPS)

Table 3. Experimental cases.

Case	Foundation (D_r)	Note
1	50%	-
2	70%	-
3	50%	Partially drained condition

Table 4. Scaling factors applied in this study.

	1g μ=1.6	Centrifuge η=50	Generalised scaling
Length	μ	η	$\mu\eta$
Density	1	1	1

Time	$\mu^{0.75}$	η	$\mu^{0.75}\eta$
Acceleration	1	η^{-1}	η^{-1}
Pressure	μ	1	μ
Permeability	$\mu^{0.75}$	η	$\mu^{0.75}\eta$
Displacement	$\mu^{1.5}$	η	$\mu^{1.5}\eta$

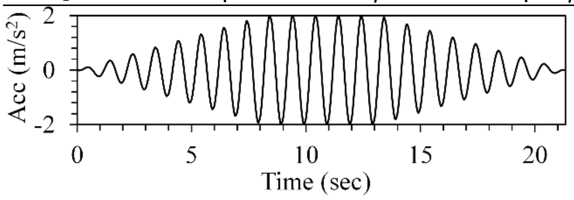

Figure 3. Input acceleration (Prototype scale).

2.2 Numerical modelling

Numerical analyses were performed using the FEM code FLIP ROSE Ver. 8.1 with the cocktail glass model of the strain-space multiple shear mechanism through parameters shown in Table 5 (Iai et al., 2011). Figure 5 presents the FE models corresponding to the experimental models (Table 3). Boundary conditions: the base is fixed, and the side are fixed only in the horizontal direction, replicating the experimental rigid box. The water level was set at the ground surface.

The model parameters for Ottawa sand, shown in Table 6, were referenced from previous studies (Vargas, 2024). Figure 5 presents the liquefaction resistance curve with 7.5% of single-amplitude shear strain (γ_{SA}). The impermeable layer was assigned the same parameters as Ottawa sand (D_r=50%), while its permeability was reduced to 3.30×10^{-7} m/s by scaling the permeability of Ottawa sand according to the ratio of the viscosities of the pore fluids (71.2 cSt for the foundation and 45,000 cSt for the impermeable layer). The embankments were modelled as non-liquefiable; liquefaction characteristic parameters were not assigned. Although Silica Sand No. 3 has a relatively low density, this corresponds to a dry state, consistent with the experimental conditions. The numerical input acceleration is identical to Figure 3.

Table 5. Model parameters for Cocktail glass model.

	Parameter designation
P_s	Confining pressure (kPa)
G_{ma}	Shear modulus (kPa)
K_{L/U_a}	Bulk modulus (kPa)
ρ_t	Mass density (Mg/m^3)
n	Porosity
ϕ_f^{PS}	Internal friction angle (°)
ϕ_P	Phase transformation angle (°)
H_{max}	Maximum damping constant
ε_d^{cm}	Limit of contractive component
$r_{\varepsilon_d^c}$	(−) dilatancy control parameter
r_{ε_d}	(+)/(−) dilatancy parameter
q_1	EPWP initial phase control parameter
q_2	EPWP final phase control parameter
l_k	K_{L/U_a} index of EPWP dissipation
r_k	K_{L/U_a} reduction factor
c_1	Lower limit of liquefaction resistance curve
k	Permeability coefficient

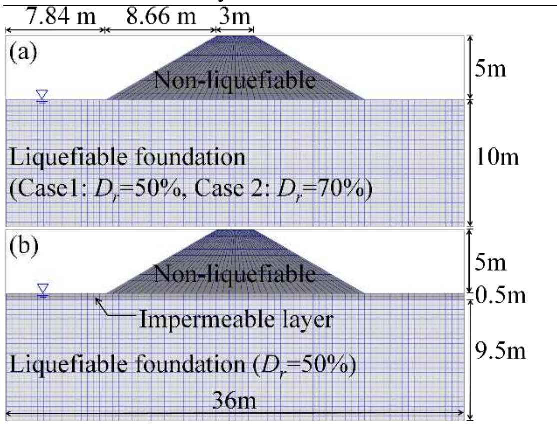

Figure 4. FE modelling and boundary conditions (a) Case 1 and Case 2 model, (b) Case 3 model.

Table 6. Model parameters for Cocktail glass model.

	Ottawa sand		Silica No. 3 sand
	D_r=50%	D_r=70%	
P_s	98	98	98
G_{ma}	75967	12300	165263
K_{L/U_a}	209270	328000	440700
ρ_t	2.02	2.05	1.5
n	0.38	0.36	0.43
ϕ_f^{PS}	38.0	41.5	42.0
ϕ_P	20.2	24.0	-
H_{max}	0.24	0.24	-
ε_d^{cm}	0.85	0.85	-
$r_{\varepsilon_d^c}$	7.5	2.5	-
r_{ε_d}	0.15	0.18	-
q_1	4.6	7.0	-
q_2	1.20	1.25	-
l_k	2	2	-
r_k	0.75	0.50	-
c_1	1.49	2.47	-
k	2.07×10^{-4}	2.07×10^{-4}	4.5×10^{-3}

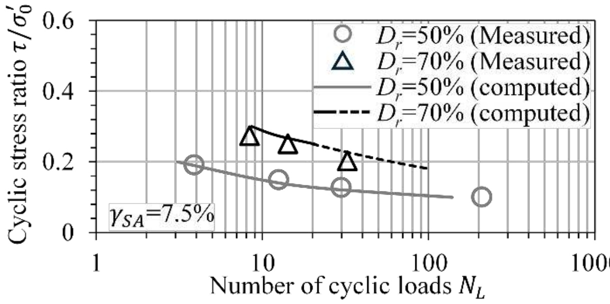

Figure 5. Liquefaction resistance curve (measured: Vargas et al., 2020; computed: this study).

3 RESULTS

3.1 Acceleration

Figure 6 presents acceleration results, including the absolute maximum amplitude. A0-A6 correspond to the sensor locations shown in Figure 2. The numerical results were extracted at the FE nodes closest to the corresponding sensor locations.

The input accelerations (A0) were well-applied across all cases. At A1, the experimental results show that the acceleration amplitude is greater in Case 1 than in Case 2, which may be due to the larger deformation induced by the lower relative density. The most significant amplitude reduction occurs in Case 3. In the experiments, restriction in the positive acceleration direction is observed due to the rigid box; however, this effect is not replicated in the simulations. In the numerical analyses, the absolute maximum acceleration amplitude is positive, indicating that motion toward the embankment is more constrained than motion toward the rigid boundary. The numerical analyses demonstrate limited agreement with the experimental results, primarily due to large deformations under low confining stress and pronounced boundary effects. Nevertheless, the timing of the dilatancy spike in Case 2 is accurately captured.

For A2, the experimental results indicate that the influence of the rigid boundary is less pronounced than at A1, which is attributed to the increased confining stress. The acceleration responses in Cases 1 to 3 are generally consistent in the experiments, with no notable differences. In contrast, the numerical analyses reveal significant dilatancy spikes in Cases 1 and 3, a phenomenon not significant in experiments. Notably, Case 2 demonstrates good agreement between experimental and numerical results.

At A3, the experimental Case 2 exhibits a distinct dilatancy spike, and the simulation shows a phase shift. A similar tendency is also observed in Case 1, though less pronounced. For Case 3, the numerical analysis shows a greater reduction in acceleration amplitude.

According to the A4, the experimental results for Cases 1 and 3 exhibit dilatancy spikes, and a similar response is observed from approximately 7 seconds in Case 2, though less pronounced than in Cases 1 and 3. In the numerical analyses, irregular amplitudes and dilatancy-related features are also reproduced with differences in waveform.

A5 shows almost perfect agreement between the experimental and numerical results for Case 2. In contrast, Cases 1 and 3 exhibits an opposite phase in the dynamic response between the experiment and the simulation.

At A6, the experimental and numerical results show relatively overall good agreement for all cases. In Cases 1 and 3, sharp spikes are observed in the experimental results after approximately 8 seconds, whereas such features are not prominent in Case 2. Numerical analyses demonstrate that the response amplitudes in Cases 1 and 3 are lower than those observed in Case 2, which suggests a more significant reduction in ground strength under conditions of lower relative density.

3.2 Excess pore water pressure (EPWP)

Figure 7 presents the experimental and numerical EPWP results during shaking together with the numerically calculated initial effective stress (σ'_0). Cases 1 and 2 on shallow free-field location (P1)

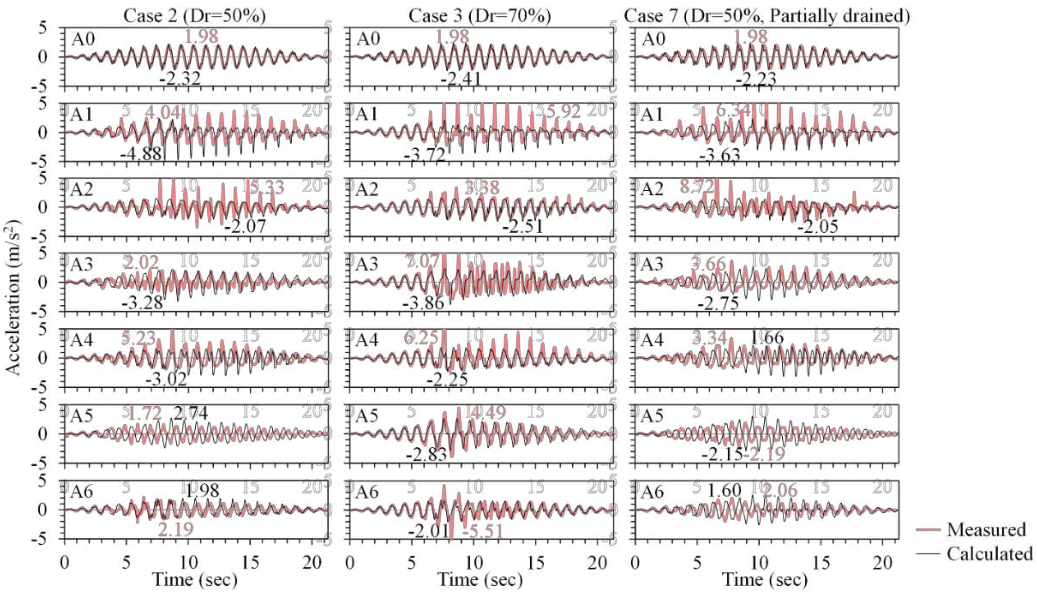

Figure 6. Time histories of experimental and numerical acceleration results.

show good agreement between the experimental and numerical results. The numerical Case 3 shows slight early-stage EPWP buildups, suggesting that the impermeable layer accelerates the shallow zone, which is relatively close to it. This tendency is consistently observed across all Case 3 results (P1, P3, and P5).

At P2, no discernible differences among the cases were observed in the experiments. In the numerical analyses, Cases 1 and 3 exhibited nearly identical responses during shaking, whereas Case 2 showed a relatively less abrupt EPWP buildup. The difference observed in the numerical analysis for Case 2 is attributed to the higher relative density. In contrast, the similar responses among the cases observed in the experiments are interpreted to result from the 1g scaling, under which the input motion has the same acceleration amplitude as that at the prototype scale (Table 4); the applied input acceleration is sufficiently strong to induce overall liquefaction regardless of relative density. Furthermore, the influence of the impermeable layer at P2 was negligible, likely due to its relatively far distance from the impermeable layer. This trend is consistently observed in both the experimental and numerical results at P2, P4, and P6.

For Case 1, differences in EPWP responses between the experimental and numerical results are observed during the early stage of shaking at all sensor locations. In the later stage of shaking, improved agreement between numerical and experimental results is observed at shallower depths, whereas at greater depths under higher embankment-induced overburden stress, the numerical analyses show EPWP behaviour that deviates from the experimental results. The same trend was observed in Case 3.

For Case 2, differences in EPWP between the experimental and numerical results are minor at shallow locations. However, differences become more evident at greater depths and beneath the embankment.

Figure 8 shows the EPWP dissipation up to 1,500 seconds, including the shaking phase, using the same format as Figure 7. During the dissipation stage, the numerical results exhibit better agreement with the experimental observations across all cases than during shaking. In Case 3, the impermeable layer has little influence on EPWP behaviour during shaking, while significantly slowing EPWP dissipation after shaking. While the magnitude of this effect varies with foundation depth and requires further investigation for quantitative evaluation, the most pronounced reduction in the EPWP dissipation rate is observed at shallower depths (P1, P3, and P5).

3.3 Deformation

Figure 9 shows the deformation configurations of experiments and numerical analyses. Experimental results are based on the model surface and soba noodles; white dot lines represent the initial configuration, and red solid lines represent the configuration after shaking. Displacements of the soba noodles are observed only in shallow regions near the embankment, with approximately 1 mm at the model scale. In other regions, displacements are too small to be clearly identified at the model scale. Case 2, with the higher relative density, exhibited the smallest settlement at the dam crest, whereas Case 3, in which an impermeable layer was applied, showed the largest dam crest settlement.

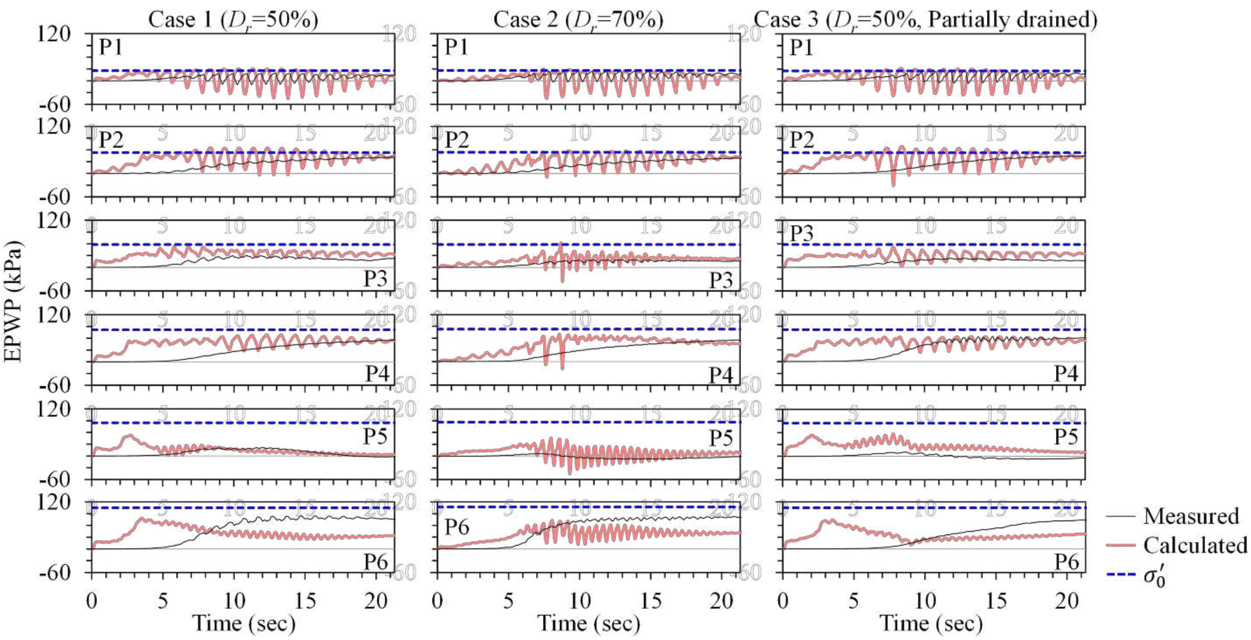

Figure 7. Experimental and numerical excess pore water pressure (EPWP) during shaking.

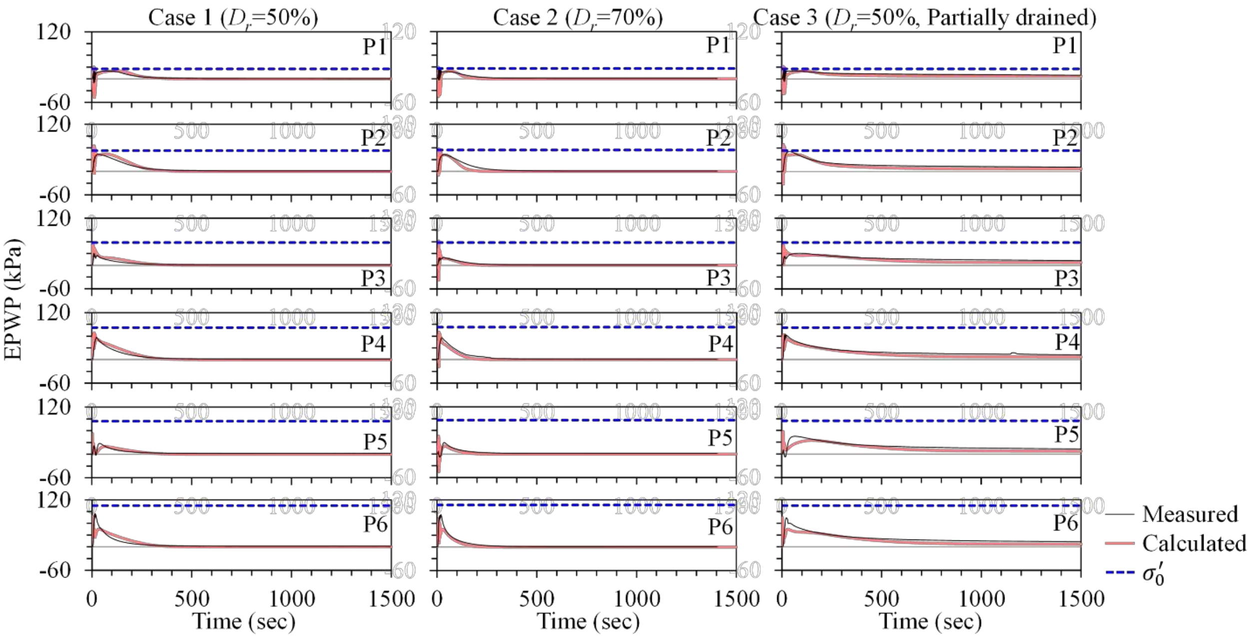

Figure 8. Experimental and numerical excess pore water pressure (EPWP) for 1,500 seconds.

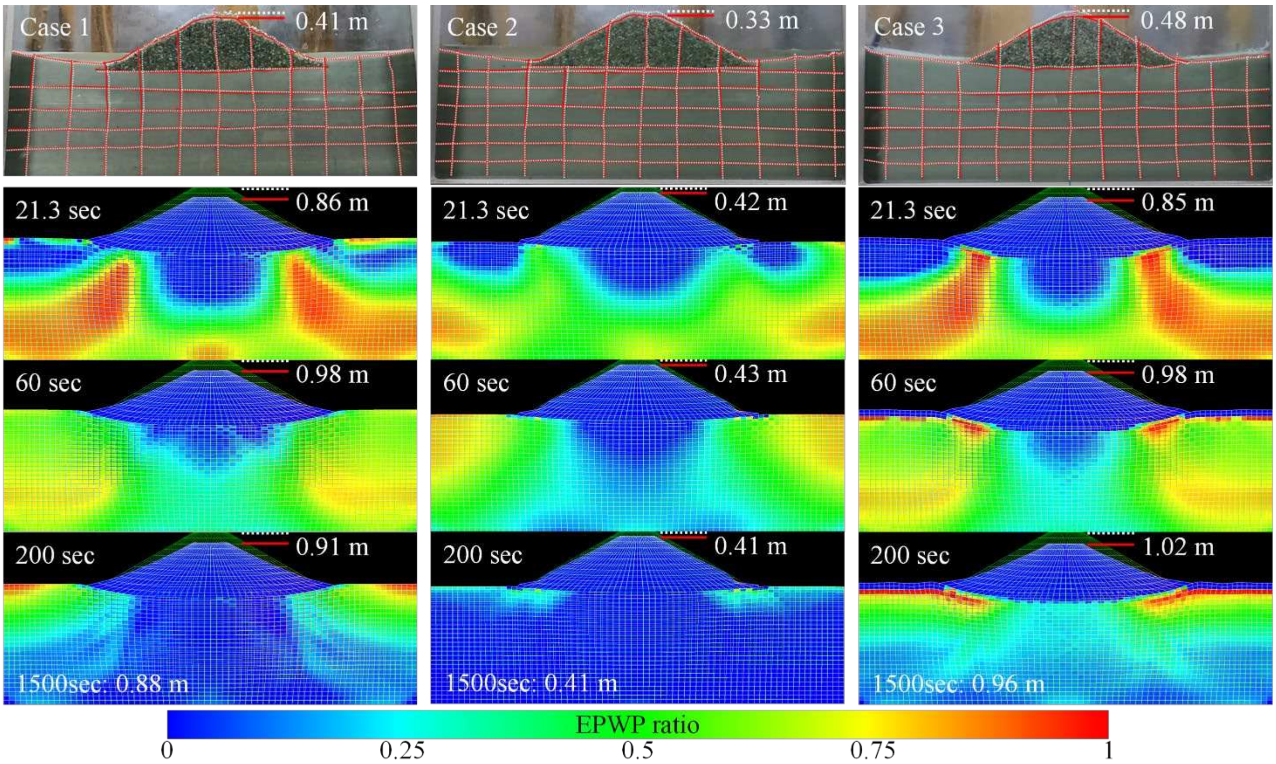

Figure 9. Deformation configurations of experiments and numerical analyses.

Numerical results are presented with time histories at the end of the shaking (21.3 seconds), 60 seconds, and 200 seconds. These time histories were selected as they are considered representative of the differences among the cases observed in the numerical analyses. In Figure 9, the dam crest settlements at 1,500 seconds were also mentioned. The numerical dam crest settlement in Cases 1 and 3 was overestimated with the experiments, whereas Case 2 exhibited a settlement that was relatively consistent with the experimental observations. Cases 1 and 2 exhibited additional settlement after shaking, followed by a slight recovery in dam crest elevation induced by ground strength recovery; this variation was more pronounced in Case 1. In contrast, Case 3, with an impermeable layer, experienced relatively larger and more prolonged post-shaking settlement, and despite some subsequent recovery of the dam crest elevation, it resulted in the largest overall settlement. In numerical Cases 1 and 3, large ground deformations were characterised by compression of the foundation soil beneath the embankment and heave of the free-field ground. The deformation behaviour of the ground in Case 2 shows good agreement with the experimental results. Furthermore, the numerical results are presented as contour plots of the EPWP ratio, which characterise the liquefaction behaviour of each case, consistent with the EPWP time-history results analysis from each numerical node.

4 DISCUSSION

4.1 Effect of the boundary condition

Discrepancies between experimental and numerical acceleration responses at A1 are attributed to boundary effects under low confining stress and differences in data extraction methods. In centrifuge experiments, accelerations were recorded by sensors embedded in the soil, potentially capturing dynamic responses associated with the sensors' mass. In contrast, numerical analyses obtained responses at nodes of a continuum finite element model. Low confining stress permits boundary-induced dynamic inertial forces to generate larger deformations during shaking, thereby amplifying discrepancies between experimental and numerical results. At greater depths, this behaviour is suppressed, leading to relatively good agreement between the experimental and numerical results at A2. These boundary effects are not directly related to the generalized scale effect and tend to produce larger discrepancies under lower relative density conditions, which are associated with greater deformation.

4.2 Relative density and overburden stress

Numerical Case 2 matched the experimental results better in acceleration, EPWP, and deformation than Cases 1 and 3. This indicates that discrepancies associated with the generalised scaling effect become less pronounced as relative density increases.

The earlier initiation of the EPWP buildup in prototype-scale numerical analyses is attributed to the lower confining stress of the generalised-scale experiments. Although the discrepancies were more evident in the lower relative density cases (Cases 1 and 3), the differences observed at greater depths in Case 2 (P4–P6) suggest an increasing influence of the generalised scaling effect on liquefaction behaviour with increasing overburden stress.

4.3 Effect of impermeable layer

In contrast to the discrepancies observed during shaking, the EPWP dissipation behaviour obtained from the numerical analyses is in close agreement with the experimental results. The minor difference observed in Case 3 may be attributed to an increase in the viscosity of the high-viscosity fluid caused by drying during the experimental modelling process, which would lead to a reduction in the effective permeability of the impermeable layer.

For Case 3 with an impermeable layer, a pronounced delay in EPWP dissipation was identified, suggesting a prolonged period of reduced ground strength compared with the other cases. This prolonged strength degradation resulted in the largest dam crest settlement in Case 3. While the duration of dam crest settlement could not be clearly quantified in the experiments, the numerical analysis indicates that the total settlement of 1.00 m in Case 3 comprises 0.85 m immediately after shaking and an additional 0.15 m during the post-shaking stage. In contrast, only about 0.01 m of post-shaking variation was observed in Cases 1 and 2.

As a surface layer with low permeability more reflects typical urban ground conditions, these results indicate that the persistence of ground strength reduction in field conditions may be underestimated when inferred solely from idealised and well-controlled experimental and numerical models.

4.4 Underestimation of deformation in centrifuge experiments

For Case 2, similar results were obtained, with a displacement of 0.33 m in the centrifuge experiment and 0.41 m in the numerical analysis. Nevertheless, it is clearly observed that the numerical analyses consistently predict larger deformations than the experiments for all cases.

Additional numerical analyses on Case 1, in which embankment density was adjusted according to the generalised scaling factor, produced deformation closer to that observed experimentally. Specifically, when the embankment density was simply reduced by a factor of 1.6 (Table 4), the crest settlement obtained from the numerical analysis for Case 1 decreased to 0.60 m. These findings indicate that the underestimation of the deformation originates from inherent differences in stress conditions induced by the generalised scaled centrifuge modelling, rather than from limitation of the numerical model.

While these differences can be adequately assessed through supplementary numerical analyses, the centrifuge experiments exhibited restricted deformation behaviour, as evidenced by the minor displacement of the soba noodles and the ground settlement. This suggests inherent limitations in generalised scaled centrifuge experiments.

5 CONCLUSIONS

This study presents numerical simulation results of centrifuge model experiments conducted at Kansai University as part of the LEAP-ASIA-2025 for a liquefiable foundation ground-embankment system. In the centrifuge experiments performed within the LEAP-ASIA-2025 framework, 1.6 times of generalised scaling laws were applied in addition to conventional centrifuge scaling laws for the model configuration, and liquefiable foundation grounds with relative densities of 50% and 70% were investigated. In addition to the LEAP-ASIA-2025 model configurations, supplementary investigations were conducted to examine liquefaction behaviour under partially drained surface conditions representative of non-liquefiable surface layer. From the present study, the following conclusions can be derived,

- Prototype numerical analyses showed good agreement with generalised scaled centrifuge experiments of acceleration response and EPWP buildup when the boundary influence decreased, the relative density increased, and the overburden stress decreased. Under such conditions, a generalised scaled centrifuge experiment provided a reasonable basis for experimental-numerical validation of liquefaction behaviour.
- The 0.5 m-thick surface impermeable layer did not induce discernible differences in liquefaction behaviour during shaking; however, it markedly reduced the rate of EPWP dissipation. Therefore, the largest dam crest settlement was observed, characterised by additional post-shaking settlement that did not occur in the cases without an impermeable layer. Since the presence of such an impermeable surface layer is considered more representative of actual urban ground conditions, the results indicate that the persistence of strength degradation in liquefied ground in real field conditions may be greater than that inferred from idealised and well-controlled experimental and numerical models.
- Deformation was consistently overestimated in the numerical analyses. Additional numerical analyses confirmed that this overestimation originates from inherent differences in stress conditions induced by the generalised scaling law of centrifuge experiments, rather than from limitations of the numerical model. These results indicate that, although the centrifuge model experiments with the generalised scaling law show good agreement with prototype-scale numerical analyses under certain conditions, it may have inherent limitations in reproducing deformation behaviours.

REFERENCES

Chiaradonna, A., Tropeano, G., d'Onofrio, A., and Silvestri, F. (2019). Interpreting the deformation phenomena of a levee damaged during the 2012 Emilia earthquake. *Soil Dynamics and Earthquake Engineering*, 124, 389-398. https://doi.org/10.1016/j.soildyn.2018.04.039

Iai, S., Tobita, T., and Nakahara, T. (2005). Generalised scaling relations for dynamic centrifuge tests. *Geotechnique*, *55*(5), 355-362. https://doi.org/10.1680/geot.2005.55.5.355

Iai, S., Tobita, T., Ozutsumi, O., and Ueda, K. (2011). Dilatancy of granular materials in a strain space multiple mechanism model. *International Journal for Numerical and Analytical Methods in Geomechanics*, 35(3), 360-392. https://doi.org/10.1002/nag.899

Kutter, B. L., Manzari, M. T., and Zeghal, M. (Eds.). (2019). Model tests and numerical simulations of liquefaction and lateral spreading: LEAP-UCD-2017. *Springer Nature*. https://doi.org/10.1007/978-3-030-22818-7

Sasaki, Y., Towhata, I., Miyamoto, K., Shirato, M., Narita, A., Sasaki, T., and Sako, S. (2012). Reconnaissance report on damage in and around river levees caused by the 2011 off the Pacific coast of Tohoku earthquake. *Soils and Foundations*, 52(5), 1016-1032. https://doi.org/10.1016/j.sandf.2012.11.018

Shin-Etsu Chemical Co., Ltd. (2005). METOLOSE.

Tobita, T., Ashino, T., Ren, J., and Iai, S. (2018). Kyoto University LEAP-GWU-2015 tests and the importance of curving the ground surface in centrifuge modelling. *Soil Dynamics and Earthquake Engineering*, 113, 650-662. https://doi.org/10.1016/j.soildyn.2017.10.012

Tobita, T., Ichii, K., and Ueda, K. (Eds.). (2024). Model tests and numerical simulations of liquefaction and lateral spreading II: LEAP-ASIA-2019. *Springer Nature*. https://doi.org/10.1007/978-3-031-48821-4

Tobita, T., Ueda, K., Vargas, R. R., Ichii, K., Okamura, M., Sjafruddin, A. N., Takemura, J.,Hang, L., Uzuoka, R., Iai, S., Boksmati, J., Fusco, A., Torres-Garcia, S., Haigh, S., Madabhushi, G., Manzari, M., Escoffier, S., Li, Z., Kim, D. S., Manandhar, S.,Hung, W.-Y., Huang, J.-X., Pham, T.-N.-P., Zeghal, M., Abdoun, T., Korre, E.,Kutter, B. L., Carey, T. J., Stone, N., Zhou, Y.-G., Liu, K., and Ma, Q. (2022). LEAP-ASIA-2019: Validation of centrifuge experiments and the generalised scaling law on liquefaction-induced lateral spreading. *Soil Dynamics and Earthquake Engineering*, 157, 107237. https://doi.org/10.1016/j.soildyn.2022.107237

Tsai, C. C., Hsu, S. Y., Wang, K. L., Yang, H. C., Chang, W. K., Chen, C. H., and Hwang, Y. W. (2018). Geotechnical reconnaissance of the 2016 ML6. 6 Meinong earthquake in Taiwan. *Journal of Earthquake Engineering*, 22(9), 1710-1736. https://doi.org/10.1080/13632469.2017.1297271

Vargas, T. R. R. (2024). Comprehensive Validation of Numerical Predictions for Liquefaction-Induced Lateral Spreading. http://hdl.handle.net/2433/288449